

Frequencies analysis of the hybrid δ Sct- γ Dor star CoRoT-102314644.

J. P. Sánchez Arias^{1,2}, O. L. Creevey³, E. Chapellier^{3*}, and B. Pichon³

¹ Astronomical Institute, Czech Academy of Sciences, Fričova 298, 25165 Ondřejov, Czech Republic
e-mail: julieta.sanchez@asu.cas.cz

² Instituto de Astrofísica La Plata, CONICET-UNLP, Argentina

³ Université Côte d'Azur, Observatoire de la Côte d'Azur, CNRS, Laboratoire Lagrange, Bd de l'Observatoire, CS 34229, 06304 Nice cedex 4, France

version: 1 June 2023

ABSTRACT

Context. Observations from space missions have allowed significant progress in many scientific domains due to the absence of atmospheric noise contributions and having uninterrupted data sets. In the context of asteroseismology, this has been extremely beneficial because many oscillation frequencies with small amplitudes, not observable from the ground, can be detected. One example of this success is the large number of hybrid δ Sct- γ Dor stars discovered. These stars have radial and non-radial p - and g -modes simultaneously excited to an observable level allowing us to probe both the external and near-to-core layers of the star.

Aims. We analyse the light curve of hybrid δ Sct- γ Dor star CoRoT ID 102314644 and characterise its frequency spectrum. Using the detected frequencies, we perform an initial interpretation developing stellar models.

Methods. The frequency analysis is obtained with a classical Fourier analysis through the Period04 package after removing residual instrumental effects from the CoRoT light curve. Detailed analysis on the individual frequencies is performed by using phase diagrams and other light curve characteristics. An initial stellar modelling is then performed using the Cesam2k stellar evolution code and the GYRE pulsation code, considering adiabatic pulsations.

Results. We detected 29 γ Dor type frequencies in the range [0.32 – 3.66] cycles per day (c/d) and a series of 6 equidistant periods with a mean period spacing of $\Delta\Pi = 1612$ s. In the δ Sct domain we found 38 frequencies in the range [8.63 – 24.73] c/d and a quintuplet centred on the frequency $p_1 = 11.39$ c/d and derived a possible rotational period of 3.06 d. The frequency analysis of this object suggests the presence of spots at the stellar surface, nevertheless we could not dismiss the possibility of a binary system. The initial modelling of the frequency data along with external constraints has allowed us to refine its astrophysical parameters giving a mass of approximately $1.75 M_{\odot}$, a radius of $2.48 R_{\odot}$ and an age of 1241 Myr.

Conclusions. The observed period spacing, a p -mode quintuplet, the possible rotation period and the analysis of the individual frequencies provide important input constraints for the understanding of different phenomena such as the transport of angular momentum, differential rotation and magnetic fields operating in A-F-type stars. Nevertheless, is fundamental to accompany photometric data with spectroscopic measurements in order to distinguish variations between surface activity from a companion.

Key words. asteroseismology, stars: oscillations, stars: variables: δ Scuti, γ Doradus, hybrid stars, techniques:photometric

1. Introduction

In the last decade, several space missions such as the COncvection ROtation and planetary Transits (CoRoT) satellite (Auvergne et al. 2009) and NASA's Kepler space telescope (Borucki 2016), have revolutionised asteroseismology, thanks to their high-precision allowing the detection of very small amplitude modes that are not detectable from ground-based instruments. Indeed δ Sct stars have been known for many decades now due to the high amplitude of some of their oscillation modes which reach up to tenths of a magnitude, while γ Dor stars are known only since 1999 (Kaye et al. 1999) and thanks to uninterrupted data from space it was possible the detection of their low amplitude periodicities near one day (Aerts et al. 2010). The existence of hybrid δ Sct- γ Dor stars has been known since 2002 (Han-

dlér et al. 2002). Their unique character of exhibiting both radial and non-radial pressure (p) oscillation modes typical of δ Sct variable stars, and gravity (g) pulsation modes characteristic of γ Dor variable stars simultaneously allows one to probe their stellar structure from the core to the envelope.

The δ Sct stars lie on and above the main sequence with masses of $1.5 - 2.5 M_{\odot}$ approximately and spectral types between A2 and F5. They exhibit radial and non-radial p - and g - modes driven by the κ mechanism operating in the He II partial ionisation zone (Baker & Kippenhahn 1962) and the turbulent pressure acting in the hydrogen ionisation zone (Antoci et al. 2014).

The γ Dor variables are generally cooler than δ Sct stars, with T_{eff} centred between 6700 K and 7400 K (spectral types between A7 and F5) and masses in the range 1.5 to $1.8 M_{\odot}$ approximately (Catelan & Smith 2015). They pul-

* Deceased on February 8th of 2022

sate in low-degree, high-order g modes apparently driven by a flux modulation mechanism called convective blocking and induced by the outer convective zone (Guzik et al. 2000; Dupret et al. 2004; Grigahcène et al. 2005). The high-order g modes ($n \gg 1$) excited in these stars, allow the use of the asymptotic theory (Tassoul 1980) and the departures from uniform period spacing to explore the possible chemical inhomogeneities in the structure of the convective cores (Miglio et al. 2008).

The aforementioned distinction between δ Sct and γ Dor stars is a topic of debate. Diverse studies on samples of δ Sct and γ Dor stars suggest that the hybrid behaviour on these stars is very common (Grigahcène et al. 2010; Uytterhoeven et al. 2011; Bradley et al. 2015; Balona et al. 2015). Moreover, in 2016, Xiong et al. (2016) calculated a theoretical instability strip using a non-local and time-dependent convection theory and concluded that the κ mechanism operates significantly in warm δ Sct and γ Dor stars while the coupling between convection and oscillations is responsible for excitation in cool stars. Furthermore, the instability strips of δ Sct and γ Dor stars partially overlap in the Hertzsprung-Russell (HR) diagram (see, for instance, Fig. 1 of Grigahcène et al. 2010), explaining the existence of hybrid δ Sct- γ Dor stars. As we mentioned, the simultaneous presence of both g and p non-radial, along with radial excited modes, allows one to place strong constraints on the whole interior structure. In addition, some of these objects show rapid rotation, making these objects excellent targets for modelling stellar structure and to test different physical phenomena such as the effect of angular transport induced by rotation (Aerts et al. 2019; Ouazzani et al. 2019).

Although a significant number of hybrid δ Sct- γ Dor stars is currently known (Grigahcène et al. 2010; Balona 2014), the analysis of low frequencies in A-F stars still represents a challenge due to the different origins that these frequencies can have, e.g. spots, field stars contaminating the light apertures of the main target, a companion forming a non-eclipsing binary system, Rossby modes usually present in moderate to rapid rotating stars and more (Li et al. 2019; Chowdhury et al. 2018; Saio et al. 2018). Our aim in this paper is to present for the first time a complete observational analysis of the light curve and the frequencies of the hybrid δ Sct- γ Dor CoRoT 102314644 along with the corresponding interpretation.

The paper is laid out as follows: both literature and CoRoT data are presented in Sect. 2, followed by the description of the frequency analysis in Sect. 3. Detailed analysis of the frequencies including their mode identification is then presented and discussed in Sect. 4. An initial interpretation of the oscillation modes with stellar models is presented in Sect. 5, and we then conclude in Sect. 6.

2. Literature data

2.1. Known stellar quantities from the literature

CoRoT 102314644 ($V \sim 12.2$, $\alpha = 6^{\text{h}}10^{\text{m}}26.73^{\text{s}}$ and $\delta = +4^{\circ}18'12.19''$) was observed during the third CoRoT long run, LRa03, which targeted the Anti-Galactic centre (see Fig 1). The observations lasted 148 days from 2009, October 10th to 2010, March 1st. The EXODAT database (Deleuil et al. 2009) indicates the star has an A5V spectral type and 2MASS photometry of $J=11.394$, $H=11.18$, $K=11.131$. It also indicates a star with reddening of $E(B-V) = 0.4$

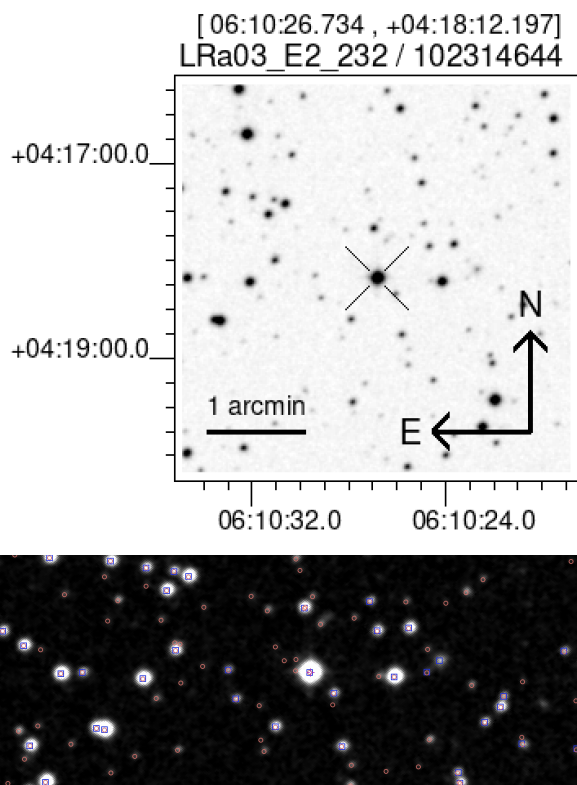


Fig. 1. Upper: Star map showing the star’s position and coordinates, from the ExoDAT database. Lower: Star map showing a slighter wider view, showing also the Gaia DR2 identified sources (red).

mag, however, more recently, Lallement et al. (2019) estimated $E(B-V) = 0.248 \pm 0.079$ mag based on the distance of the star ¹. The sky map given by the CoRoT database is shown in Fig. 1 upper panel which clearly identifies the target. We also give a wider angle sky map showing our target at the centre and the positions of Gaia Data Release (GDR2/GDR3) identified sources (Gaia Collaboration et al. 2018, 2021, 2022).

The photometry and various identifications of the star are given in Table 1.

2.2. Fundamental stellar parameters

Gaia eDR3 also provides additional properties of the star: its parallax π , its radial velocity v_{rad} and photometry G , G_{BP} and G_{RP} , given in Table 1. For π we applied the recommended parallax zero-point correction of -0.027 mas based on the magnitude, colour and sky position of the star (Lindgren et al. 2021). Using the extinction, we dereddened the photometry and used the colour- T_{eff} relations from Casagrande et al. (2020) to derive T_{eff} . To convert the extinction from $E(B-V)$ to other bands, we assumed a reddening law $R = 3.1$ and we used the coefficients from Danieliski et al. (2018). The colour- T_{eff} relations require $\log g$ and $[\text{Fe}/\text{H}]$ as input, and so we used $\log g = 3.9$ (see below) and assumed solar metallicity in the absence of literature values. Then, using G , extinction A_G , the parallax and a bolomet-

¹ <https://stilism.obspm.fr/reddening?frame=galactic&vlong=204.3733&ulong=deg&vlat=-7.104248&ulat=deg&valid=>

Table 1. Identification and literature data for CoRoT 102314644.

Parameter	Value	Ref.
Id	CoRoT 102314644	
	GDR2 3317411131453435008	
	GEDR3 3317411131453435008	
	USNO-A2 0900-02423283	
	2MASS 06102674+0418122	
α [deg]	92.611376	1
δ [deg]	+4.303372	1
α [hr mn ss]	6h 10m 26.73 s	
δ [hr mn ss]	+4h 18m 12.19s	
l [deg]	204.373325	
b [deg]	-7.104326	
Spectral Type	A5V	2
$E(B-V)$ [mag]	0.248 ± 0.079	3
C [mag]	12.3779	
R [mag]	12.3779	
J [mag]	11.394 ± 0.023	
H [mag]	11.18 ± 0.023	
K [mag]	11.131 ± 0.023	
G [mag]	12.451	1
G_{BP} [mag]	12.7584	1
G_{RP} [mag]	11.977113	1
$G_{BP} - G_{RP}$ [mag]	0.781295	
v_{rad} [km s ⁻¹]	32.9 ± 10.2	4
π_{GEDR} [mas]	0.988 ± 0.013	1
π_{sys} [mas]	-0.271	5

References: ¹Gaia Collaboration et al. (2021), ²Deleuil et al. (2009), ³Lallement et al. (2019), ⁴Gaia Collaboration et al. (2018), ⁵Lindegren et al. (2021)

ric correction, we calculated the luminosity, L . Using the Stefan-Boltzmann law with these values we estimated the stellar radius. Finally, using an estimate of mass between 1.7 and 2.1 M_{\odot} we calculated a surface gravity of 3.9 ± 0.1 using the derived radius.

T_{eff} and L are highly correlated because they both depend on the extinction value. To calculate the uncertainties and correlations in the T_{eff} L plane, we performed simulations where we perturbed the input values ($E(B-V)$, π , G , G_{BP} , and G_{RP}) by their errors. Then we propagated these perturbed values to the T_{eff} , L , radius, and $\log g$. The values obtained for L and T_{eff} are in agreement with the assumption of the star being a hybrid γ Dor- δ Scuti. The derived values and their 1-D uncertainties are: $L_{\star} = 13.6 \pm 2.9 L_{\odot}$; $T_{\text{eff}} = 7065 \pm 460$ and $R_{\star} = 2.27 \pm 0.07 R_{\odot}$. In our interpretation of the models in Sect. 5 we used these values as a first approximation to constrain the models².

2.3. CoRoT Light curve

We followed a similar analysis of this CoRoT light curve to that performed in Chapellier et al. (2012) and Chapellier & Mathias (2013). We used the reduced N2 light curves from Auvergne et al. (2009). The light curve consists of a total of 386 381 measurements obtained with a temporal resolution

² Since the finalisation of the work, Gaia DR3 proposes $L/L_{\odot} = 11.9 \pm 0.4$ and $T_{\text{eff}} = 6842^{+300}_{-200}$ K which are in good agreement with ours, and the slight differences have little impact on the results.

of 32 s. We retained only 342 598 points, those flagged as "0" by the CoRoT pipeline that were not affected by instrumental effects such as stray-light or cosmic rays. We then corrected the measurements by long-term trends (systematic trends). Individual measurements considered outliers (primarily high-flux data points caused by cosmic ray impacts) were removed by an iterative procedure. We retained a total of 340 257 measurements in total, which gives an approximate frequency resolution of 0.008 c/d.

The resulting light curve is represented at different timescales in Fig. 2. The amplitude has been calculated by converting from flux to magnitudes and subtracting the mean. The timescale is labelled in units of the CoRoT Julian day (JD), where the starting CoRoT JD corresponds to HJD 2445545.0 (2000, January 1st at UT 12:00:00). On the top panel, we show the full corrected light curve spanning 148 days. In the middle and lower panels, we show 20 and 5 days time spans, respectively. Here we can distinguish two kinds of periodic time scales: one corresponding to low frequencies, characteristic of γ Dor stars (middle panel), and one due to higher frequencies, which are characteristic of the δ Sct star (lower panel).

3. Light curve analysis

We analysed the frequency content of the light curve using the package Period04 (Lenz & Breger 2005). We searched frequencies in the interval [0;100] c/d. For each detected frequency, the amplitude and the phase were calculated by a least squares sine fit. The data were then cleaned of this signal (this is known as pre-whitening) and a new analysis was performed on the residuals. This iterative procedure was continued until we reached the signal to noise (S/N) equal to 5.2 as it is recommended (Baran & Koen 2021). The first Fourier transform in the range 0 – 30 c/d is depicted in Fig. 3, with the y-axis showing amplitude.

We eliminated frequencies lower than 0.25 c/d. These correspond to trends in the CoRoT data (Chapellier et al. 2012), and the satellite orbital frequency ($f_{\text{sat}} = 13.97213$ c/d) along with its harmonics. In addition, small-amplitude frequencies with a separation from large-amplitude frequencies less than the frequency resolution were ignored. These smaller amplitude frequencies are not real and are due to the spectral window or to amplitude or frequency variability of the pulsations during the observations (Bowman et al. 2016).

As a result, we obtained a total of 68 stellar frequencies. The first 10 frequencies with the highest amplitude are shown in Table 2 and the complete list with uncertainties is given in Tables A.1 and A.2.

We also included in Tables A.1 and A.2 an identity for each frequency (see next Section). Briefly, we identified two ranges of frequencies: δ Sct and γ Dor frequency ranges, which are labelled with "p" and "g", respectively; and the frequency with the highest amplitude in each range has the sub-index "1" and subsequent frequencies with lower amplitudes are labelled with increasing sub-index.

The uncertainties in the frequencies were calculated by performing Monte-Carlo-like simulations on the light curve and recalculating the frequency content of each simulated light curve. More concretely, we created a fake signal s_j by adding background noise to the original signal. We calculated the periodogram and then fit the individual frequencies of the simulated periodogram. The fit to each frequency

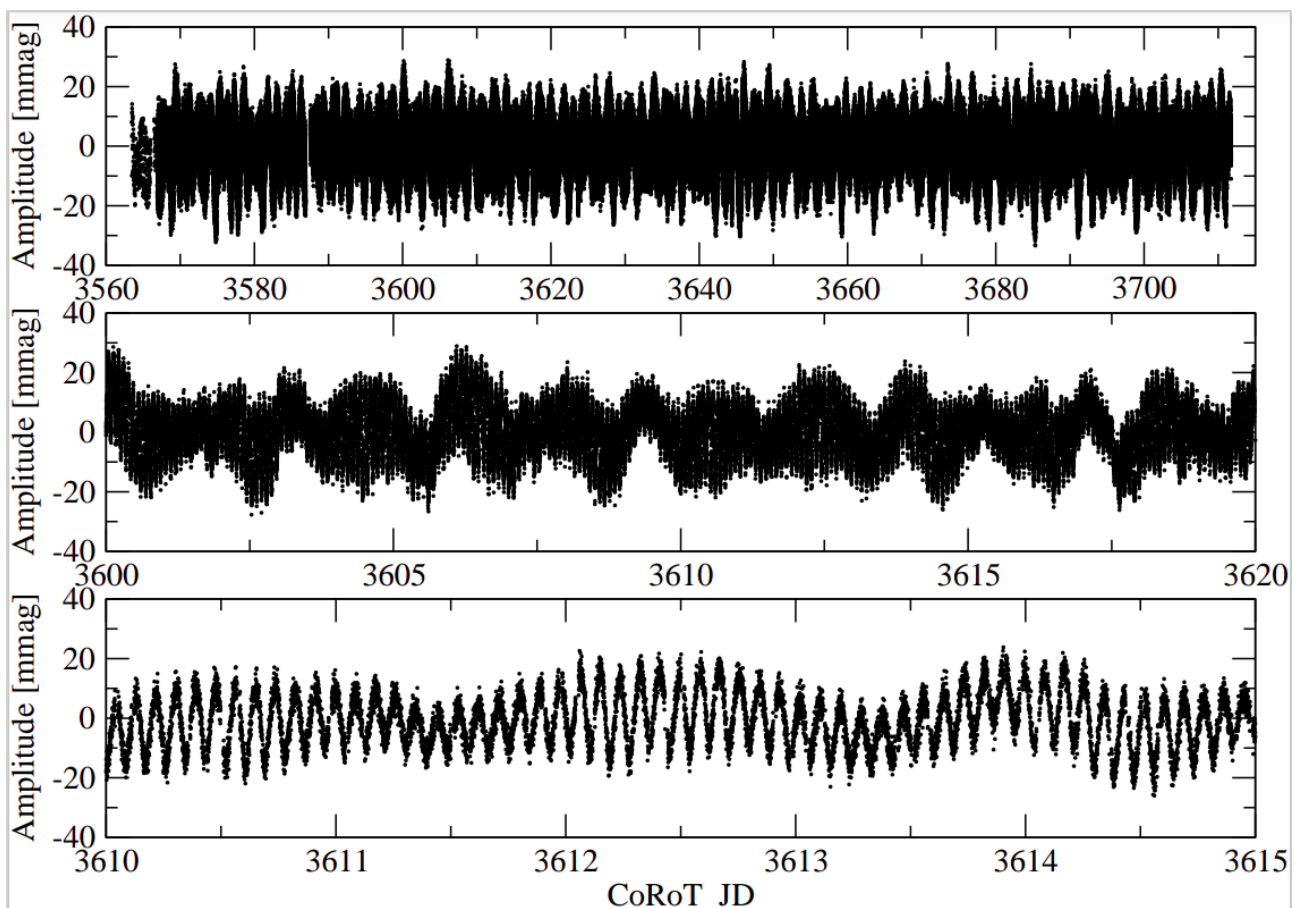


Fig. 2. Light curve of the star CoRoT 102314644 corrected for long-term trends and outliers (see text) for different timescales. From top to bottom, the complete light curve over 148d, then a set over 20 d and finally a zoom into 5 d subset.

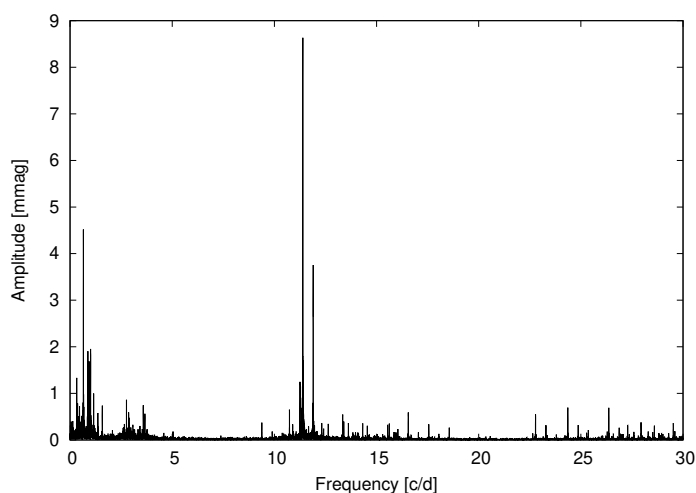


Fig. 3. First Fourier transform of CoRoT 102314644.

$f_{j,i}$, where i runs over the list of independent frequencies, was retained for each $j = 1, \dots, N$ simulation. We used $N = 500$ as this provided a good balance between computation time and enough sampling. We then analysed the resulting distributions of each f_i , by calculating the 68%, 95% and 99.7% confidence intervals. We checked first that these values scaled roughly as we expect them to. We report the

Table 2. List of the first ten frequencies with the highest amplitudes.

	Frequency [c/d]	Amplitude [mmag]	Phase Φ [rad]	Ident
F_1	11.39107	8.680	0.991701	p_1
F_2	0.65259	4.470	0.819798	$2f_{rot}$
F_3	11.89972	3.726	0.572764	p_2
F_4	1.00595	2.002	0.601673	g_1
F_5	0.87286	1.881	0.772675	g_2
F_6	0.90251	1.522	0.581354	g_3
F_7	0.93445	1.496	0.237861	g_4
F_8	0.32629	1.374	0.489074	f_{rot}
F_9	0.88683	1.238	0.682482	g_5
F_{10}	11.25403	1.165	0.117229	p_3

99.7% interval ($\sim \pm 3\sigma$) in the second column in Tables A.1 and A.2 .

4. Analysis of extracted frequencies

We analyze the frequencies derived in Sect. 3 and we distinguish four main regimes to discuss: δ Set type frequencies, γ Dor type periods, a regime with a coupling of “p” and “g” modes, and frequencies whose nature we discussed in terms of surface activity or gravitational effects provoked by a companion. One of the tools we used for the analysis

of the frequencies is the phase diagram. The construction of these diagrams consists in taking all the observations and folding the light curve modulo a single standardized period (in time). Each time point is then assigned a phase with respect to this chosen period, and it takes a value of between 0 and 1, ($0 < \phi < 1$). All measurements are then plotted with phase as the independent variable.

4.1. Spots or binarity?

We noted that the first low frequency $F_2 = 0.65259$ c/d with $A = 4.47$ mmag has a half frequency harmonic $F_8 = 0.32630$ c/d with $A = 1.37$ mmag. Such a combination of a frequency and a lower amplitude half frequency corresponds to a double wave curve typical for spotted or eclipsing stars (see e.g. Paunzen et al. 2017). Figure 4 shows the phase diagram corresponding to $F_8 = 0.32630$ c/d after removing all frequencies corresponding to pulsation modes (see Sect. 4.2 and 4.3). It clearly shows a double wave curve which can be explained in terms of spots or a companion of an ellipsoidal variable, assuming that $F_8 = 0.32630$ c/d is the orbital frequency. In the case of spots, the star appears slightly fainter when a large dark spot is on the visible side, and slightly brighter when it is not. Note that the phase diagram corresponding to the rotation frequency in a regular single star without pulsation frequencies or surface activity, should be flat. A similar effect would be produced by a companion in an ellipsoidal variable system. These systems are non-eclipsing close binaries whose components are distorted by their mutual gravitation and the variations observed in the light curve are due to the changing variations are therefore due to the changing cross-sectional areas and surface luminosities that the distorted stars present to the observer at different phases (Morris 1985).

We explored the possibility of being in the presence of one of these systems. We followed the equations in Morris (1985) assuming $P = 3.06$ d, $R_1 = 2.27R_\odot$ as derived in Sec. 2.2, $M_1 = 1.75M_\odot$, $\tau = 0.2$ and $\mu = 0.4$ from Claret & Bloemen (2011) and $\Delta m = 0$. We found possible solutions for a mass companion, resulting impossible to dismiss this hypothesis, for example, $M_2 = 0.7M_\odot, 1.4M_\odot$ for $A = 12R_\odot, 13R_\odot$ respectively, being A the semimajor axis.

With the aim to explore the existence of spots, we examined the behaviour of the star over several rotational periods, assuming a rotational frequency equal to $F_8 = 0.32630$ c/d (~ 3.06466 d). We binned the data of the light curve in groups of ten measurements by assigning the average in time and magnitude to each group, and then we pre-whitened the data with all the pulsational frequencies. The result is presented in Fig. 5 for the duration of 3 rotational periods, each of them separated with horizontal lines. Two phenomena are present: amplitude variations from one orbit to another and moving bumps. The moving bumps might be explained by spots located at different latitudes. Additionally, the changes shown in Fig. 5 can be due to spots with a short lifetime. In the Sun, for example, the lifetime of the spots can vary between hours to months and it is known that they usually migrate (Solanki 2003). Besides, it has been shown that for hot stars the lifetime tends to decrease, especially for those stars with short rotational periods (Giles et al. 2017) as the case of CoRoT 102314644. This suggests that CoRoT 102314644 can be a spotted star with a rotation period of $P_{rot} = 3.0647$ d. Nevertheless, we found frequencies (F_{49}, F_{55} and F_{64}) that are linear com-

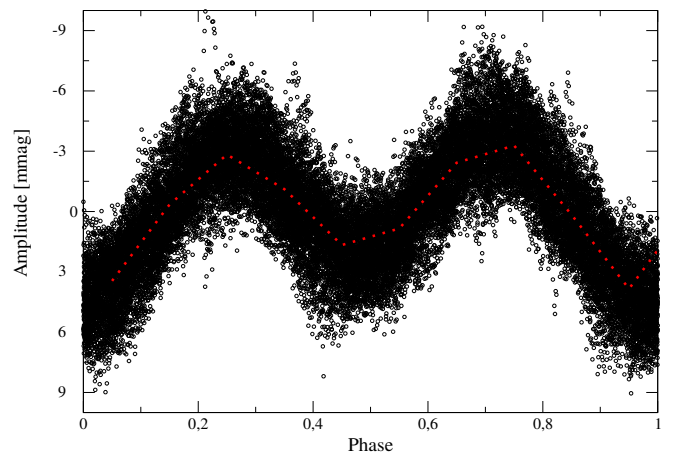


Fig. 4. Phase diagram using the rotational frequency $f_{rot} = 0.326$ c/d after removing of all the pulsational frequencies.

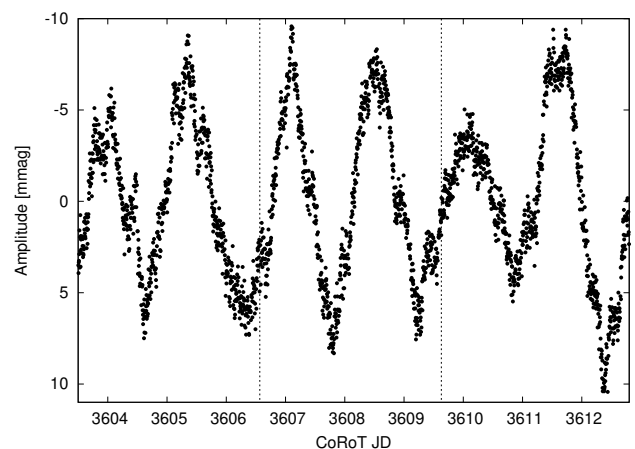


Fig. 5. Extract of the light curve corresponding to three rotational periods separated with vertical lines. We used the residuals after removing all pulsational frequencies of the binned data.

ination of f_{rot} and this strongly suggest that the origin of f_{rot} is not surface activity (Kurtz et al. 2015) but, possibly, the beating of undetected pulsation frequencies. In order to determine properly the origin of these variabilities, spectroscopic measurements are required.

4.2. γ Doradus domain

We found a total of 29 frequencies in the range of $0.3262 - 3.6631$ c/d. From these frequencies, those we consider g -modes oscillations are labelled as “g” modes in Tables A.1 and A.2. The frequency with the highest amplitude in this domain, after $F_2 = 2f_{rot}$, is $F_4 = 1.0059$ c/d with $A = 2.0$ mmag.

Light variabilities from orbital or rotational variation are typically non-sinusoidal, thus, in order to distinguish between possible real g -modes and the frequencies corresponding to the spots in this domain, we analyse the phase diagram for each frequency. The phase diagrams for typical g and p modes frequencies have a sinusoidal behaviour. For instance, in Fig. 9 we have folded the light curve at the period corresponding to F_1 , and here we can clearly observe

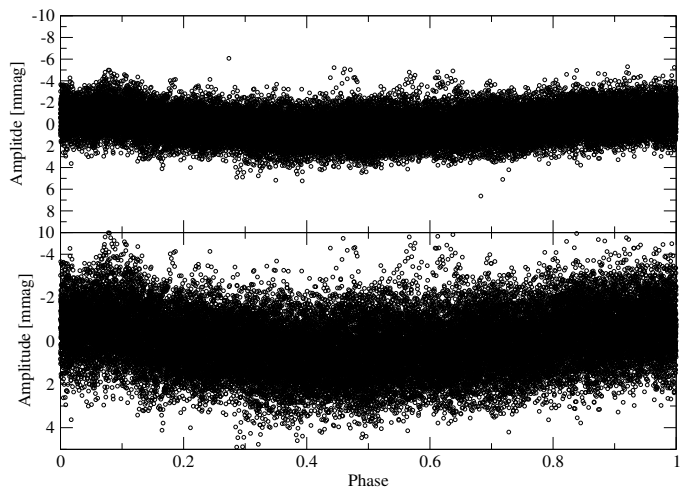


Fig. 6. Data phased with $F_{18} = 0.46385$ c/d, a frequency possible related to spots in the γ Doradus domain using different scale ranges.

sinusoidal behaviour. This suggests that F_1 is an oscillation eigenmode. On the other hand, for $F_{18} = 0.4638$ c/d, a non-sinusoidal can be spotted. In Fig. 6 the phase diagram for F_{18} for different amplitude scales is depicted. It seems that there is a maximum around 0.1 and a minimum between 0.3 and 0.4. This suggests that F_{18} may correspond to periods related to spots. Nevertheless, we note that this test provides only hints about the origin of the frequency and is not conclusive. In fact, if F_{18} were originated by spots, it would imply over 40% in differential rotation, which is a value slightly high for A-F stars (Reinhold et al. 2013).

Considering F_{18} as originated from spots and dismissing the rotational frequency and its harmonics, we retain a total of 26 frequencies in the γ Doradus domain, possibly g -modes, depicted in black in Fig. 7. In addition, we searched for frequency combinations in this range, but no frequency couplings or splittings were found among these g -modes. We labelled the frequencies ' F_k ' as a combination of frequencies after finding a fit of at least two significant digits among all the possible combinations of type ' $mF_i \pm nF_j$ ', for the given frequency ' F_k '.

Hybrid δ Sct- γ Dor stars, as well as γ Dor stars, are characterised by having high-order g modes. For these modes, with high radial order (k) and long periods, the separation of consecutive periods ($|\Delta k| = 1$) becomes nearly constant and it depends on the harmonic degree (ℓ), given the asymptotic theory of non-radial stellar pulsation (Tassoul 1980) in which the asymptotic period spacing is:

$$\Delta\Pi_\ell = \frac{\Pi_0}{\sqrt{\ell(\ell+1)}}, \quad (1)$$

with

$$\Pi_0 = 2\pi^2 \left(\int_{r_1}^{r_2} N \frac{dr}{r} \right)^{-1}, \quad (2)$$

where r is the distance from the stellar centre, N is the Brunt-Väisälä frequency and r_1 and r_2 are the boundaries of the propagation region.

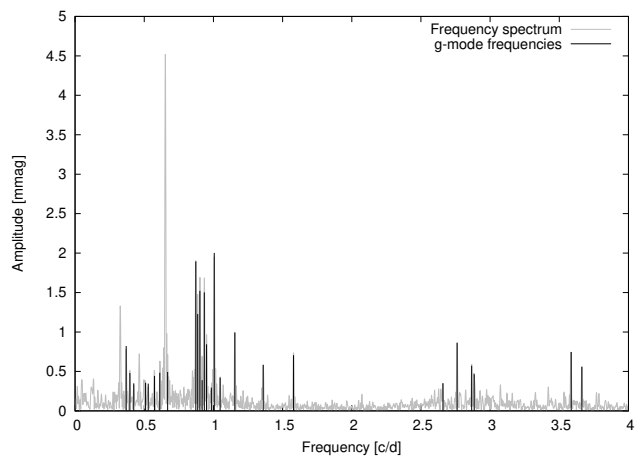


Fig. 7. Amplitude versus frequency in the γ Dor range of [0:4] c/d. Black lines represent all the g -mode frequencies found in this range. Grey data corresponds to the frequency spectrum obtained from the FT.

Table 3. List of the six periods of the asymptotic series.

	Period [sec]	A [mmag]	Ident
F_{14}	90878.5	0.841	g_8
F_7	92460.8	1.496	g_4
F_{32}	94061.3	0.387	g_{19}
F_6	95733.0	1.522	g_3
F_9	97425.6	1.238	g_5
F_5	98984.9	1.881	g_2

Motivated by this fact, we searched for equidistant γ Dor periods, by analysing the differences between all the periods found in the γ Dor domain. We found a series of 6 equidistant periods with a mean separation of $\Delta\Pi = 1621$ sec (see Table 3). These periods correspond to g -modes of the same harmonic degree ℓ and consecutive radial orders k . The asymptotic series is depicted in Fig 8. In the top panel of this figure, we show the periods (Π) versus an arbitrary radial order (k). We can see that these periods are almost equally spaced forming a line. In the bottom panel of this figure, we show the forward period spacing ($\Delta\Pi = \Pi_{k+1} - \Pi_k$) versus k , and we denote the corresponding average period spacing with the red horizontal continuous line. According to Van Reeth et al. (2016), the value we found is more likely to correspond to an asymptotic series with $\ell = 2$. In this paper the authors determine values of about 3100 s and 1800 s for the asymptotic period spacing calculated with $\ell = 1$ and $\ell = 2$ respectively, employing Eq. 1 and 2. In fact, our models predict a harmonic value $\ell = 2$ for this series.

4.3. δ Scuti domain

In the δ Scuti domain, we found a total of 38 frequencies in the range 8.6 – 24.73 c/d. The highest amplitude frequency in this range is $F_1 = 11.3910$ c/d with $A = 0.008$ mag. A phase diagram folded with this frequency shows sinusoidal behaviour (Fig. 9), indicating thus that F_1 is an eigenmode.

Stellar rotation induces rotational splitting of the frequencies in the pulsation spectra. Considering rigid rotation

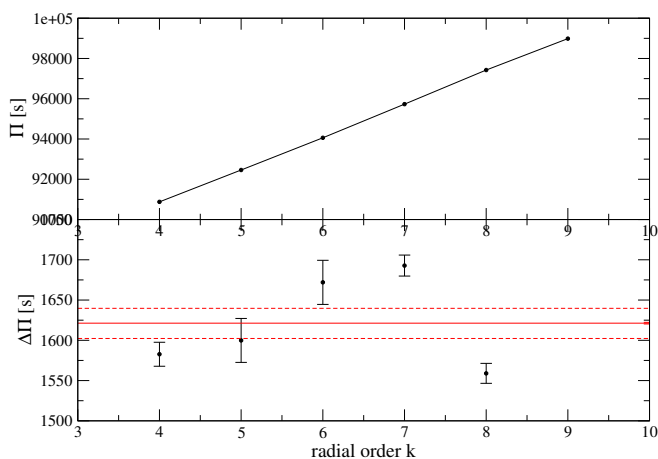


Fig. 8. Top Panel: Period versus an arbitrary radial order for the equally spaced series of periods founded. Bottom panel: forward period spacing versus radial order. The horizontal red line indicates the average period spacing along with the associated error in dashed lines.

Parameter	Value
$\Delta\Pi$	1621 s
P_{rot}	3.064 d
p-mode	labelled as ' p_i ' in Tables A.1 and A.2
g-mode	labelled as ' g_i ' in Tables A.1 and A.2
p-g-modes	see Table 7
quintuplet	see Table 5

Table 4. Summary of the variable content of the star.

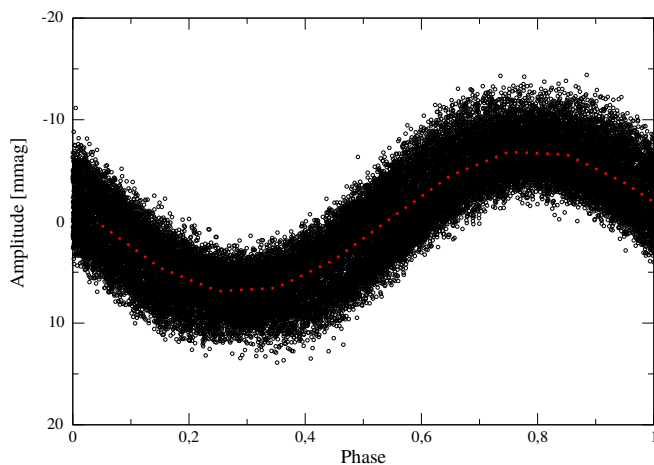


Fig. 9. Data phased with $F_1 = 11.3910$ c/d, the highest amplitude frequency in the δ Scuti domain.

and the first-order perturbation theory, the components of the rotational multiplets are:

$$\nu_{nlm} = \nu_{nl} + m(1 - C_{nl}) \frac{\Omega}{2\pi} \quad (3)$$

where ν_{ln} is the central mode of the multiplet and $\Omega/2\pi$ is the rotational frequency. We found a quintuplet centred on $p_1 = F_1$ (see Table 5), which clearly indicates that this frequency is a non-radial mode with $\ell = 2$. The differences

Table 5. List of frequencies of the quintuplet.

	Frequency [c/d]	A [mmag]	Ident	$p_1 - F_i$ [c/d]
F_{19}	10.73844	0.667	$p_1 - 2f_{\text{rot}}$	0.65263
F_{63}	11.06506	0.081	$p_1 - f_{\text{rot}}$	0.32601
F_1	11.39107	8.680	p_1	–
F_{58}	11.71775	0.083	$p_1 + f_{\text{rot}}$	-0.32668
F_{47}	12.04353	0.133	$p_1 + 2f_{\text{rot}}$	-0.65246

Table 6. List of combinations between p modes and harmonics.

	Frequency [c/d]	A [mmag]	Phase [rad]	Ident
F_{38}	23.29078	0.306	0.938	$p_1 + p_2$
F_{46}	22.64486	0.143	0.362	$p_1 + p_3$
F_{48}	22.80735	0.125	0.498	$p_1 + p_4$
F_{66}	24.73414	0.052	0.559	$p_1 + p_5$
F_{23}	22.78214	0.539	0.406	$2p_1$
F_{52}	23.79931	0.102	0.865	$2p_2$

between the central mode and the components of the quintuplets are given in the last column of Table 5. Considering $C_{nl} \approx 0$ for p modes, we find a very good agreement with the value for $f_{\text{rot}} = 0.32629$ c/d derived in Sec. 4.1. However, this match does not dismiss the possibility of CoRoT 102314644 being an ellipsoidal variable. In fact, an alternative interpretation of this splitting would be tidally deformed oscillation modes that have variable amplitude over the orbit, in case 0.32629 c/d is indeed a binary orbital period.

We also found 4 combinations between p modes exclusively, and the harmonics for p_1 and p_2 (see Table 6). The linear combination between two frequencies, yields a third frequency whose amplitude is smaller than those that form it. It is important to distinguish between mode-coupled frequencies from "pure" frequencies because when developing asteroseismic modelling, only frequencies that come from pulsation, i.e. "pure" frequencies can be accurately calculated and thus used.

Removing the couplings, the harmonics and the splitting corresponding to p_1 , we retain a total of 15 independent frequencies in the range of 10.9 – 21.4 c/d, depicted in black in Fig. 10.

4.4. P and g modes combinations

The coupling between p and g modes was originally proposed as a way to explore g modes in the Sun, see Kennedy et al. (1993) and more recently Fossat et al. (2017). According to these studies, internal solar g -modes produce frequency modulation of p -modes which results in a pair of side-lobes symmetrically placed about each p -mode frequency. We explored this feature of g -modes in p -modes by searching combinations of frequencies in the δ Sct domain. We found these combinations in the form of $p_1 \pm g_i$, with $i = 1, 2, 3$ and $p_1 - g_4$ and $p_1 - g_7$. The list of coupled p and g modes is given in Table 7. This same interaction has also been found in two other hybrid stars, namely, CoRoT-100866999 and CoRoT-105733033 studied in detail in Chapellier & Mathias (2013) and Chapellier et al. (2012), respectively. This indicates that the coupling mechanism

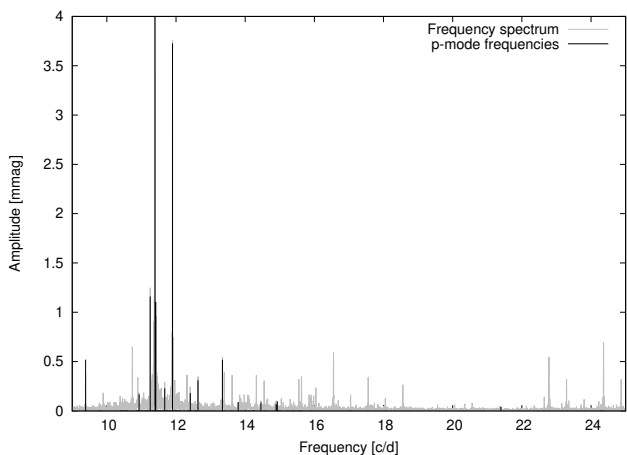


Fig. 10. Amplitude versus frequency diagram zoomed into the δ Sct range of [10 – 25] c/d. Black lines represent the pure p mode frequencies found in this range. Grey data corresponds to the frequency spectrum obtained from the FT.

Table 7. List of p and g mode coupling for the highest amplitude frequency.

	Frequency [c/d]	A [mmag]	Ident
F_{50}	10.38536	0.113	$p_1 - g_1$
F_{55}	12.39788	0.0920	$p_1 + g_1$
F_{49}	10.51816	0.115	$p_1 - g_2$
F_{54}	12.26440	0.096	$p_1 + g_2$
F_{62}	10.48902	0.0808	$p_1 - g_3$
F_{60}	12.29424	0.0836	$p_1 + g_3$
F_{57}	10.45718	0.0881	$p_1 - g_4$
F_{59}	8.62954	0.0848	$p_1 - g_7$

first proposed by Kennedy et al. (1993) also operates in hybrid δ Sct and γ Dor stars.

It is important to notice that the detection of a combination between p and g -modes, i.e. $p_i \pm g_j$, implies that p_i and g_j originated in the same star.

Additionally, we found one frequency between the δ Sct and γ Dor domains, $i_1 = 5.038$ c/d in Table A.1, whose position in the frequency spectrum did not allow us to safely classify them.

5. Interpretation of frequency data

5.1. Rotational period and critical velocity

The analysis of low frequencies in A-F stars is a tricky task. It requires several considerations, especially when analyzing hybrid pulsators and this problem arises not only with CoRoT observations but also with TESS data. Many phenomena can mimic stellar oscillations and additional data than photometry is required to disentangle the possible phenomena (Skarka et al. 2022).

In Sec. 4.1 we interpreted the period found $P_{\text{rot}} = 3.064$ d, or $f_{\text{rot}} = 0.326$ c/d in two different ways: the rotational period of the star or the orbital period of a binary system. Given that the splitting found can also be interpreted as tidally deformed oscillation modes that have variable amplitude over the orbit of a binary system, we could not rule

out the possibility of CoRoT 102314644 being a binary system.

With the aim to test further the case of a single star, we calculated the rotational and critical velocities for the values obtained in Sec. 2. By considering the estimated radius, $R_* \sim 2.27R_{\odot}$, we obtain a linear rotational velocity ($v = 2\pi R/P_{\text{rot}}$) of ~ 37 km s $^{-1}$. In this case, the corresponding rotational critical velocity ($v_{\text{crit}} = \sqrt{GM_*/R_*}$) for a mass of $1.75M_*$ would be ~ 383 km s $^{-1}$, meaning that the linear velocity is less than 10% of the critical velocity.

The effect of rotation in main sequence stars varies parameters involved in the modelling of stars such as the mean period spacing and the splitting of p -modes even at linear velocities which are a low percentage of the critical velocity. Nevertheless, in this work, we present a preliminary model of CoRoT 102314644 without considering rotation, as a first approximation.

5.2. Use of stellar models to constrain the mass and age

With the aim to perform a preliminary modelling of CoRoT 102314644 we first explore the position of this star in the HR diagram for masses and overshooting parameters.

The stellar structure and evolution models were calculated with Cesam2k code (Morel & Lebreton 2008)³. We considered masses between 1.5 and $1.8M_{\odot}$ with a mass step of $0.05M_{\odot}$ and overshoot parameters of $\alpha = 0.0, 0.1$ and 0.3 . Overshooting phenomena were considered as an extent of the chemical mixing region around the convective core through the expression for the overshooting distance:

$$d_{OV} = \alpha_{OV} \times \min(H_P, r_S) \quad (4)$$

where H_P is the local pressure scale height and r_S is the Schwarzschild limit of the core.

Fig. 11 shows the HR diagram with the evolutionary sequences for different masses and overshooting parameters from the pre-main sequences up to an abundance of H of 10^{-6} in the core, along with the error boxes centred on the values of $\text{Log}(L/L_{\odot})$ and $\text{Log}(T_{\text{eff}})$ derived in Sec. 2.

In order to find a representative model for CoRoT 102314644, we selected different models indicated with circles inside the box shown in Fig. 11, and then we calculated their oscillation modes with GYRE code (Townsend & Teitler 2013). We computed adiabatic radial and non-radial ($\ell = 0, 1$ and 2) p - and g -modes in the frequencies range [0.3, 23] c/d, thus encompassing the range of observed frequencies.

³ The following physics were considered: The opacities are those from Iglesias & Rogers (1996) and Alexander & Ferguson (1994), we used the equation of state of OPAL project (Rogers et al. 1996) and a nuclear network with the following elements: ^1H , ^2H , ^3He , ^4He , ^7Li , ^7Be , ^{12}C , ^{13}C , ^{14}N to describe the H (proton-proton chain and CNObi-cycle), and He burning and C ignition with reaction rates extracted from (Angulo et al. 1999). In addition, we adopted the classical mixing length theory (MLT) (Böhm-Vitense 1958) for convection with a free parameter $\alpha = 1.85$. The occurrence of diffusion and mass loss during the evolution was dismissed and the solar metallicity distribution considered Grevesse & Sauval (1998). We used MARCS atmosphere models (Gustafsson et al. 2008). All of our models have an initial H and He abundances per mass unit of 0.72 and 0.26 with an initial value $Z/X = 0.0028$.

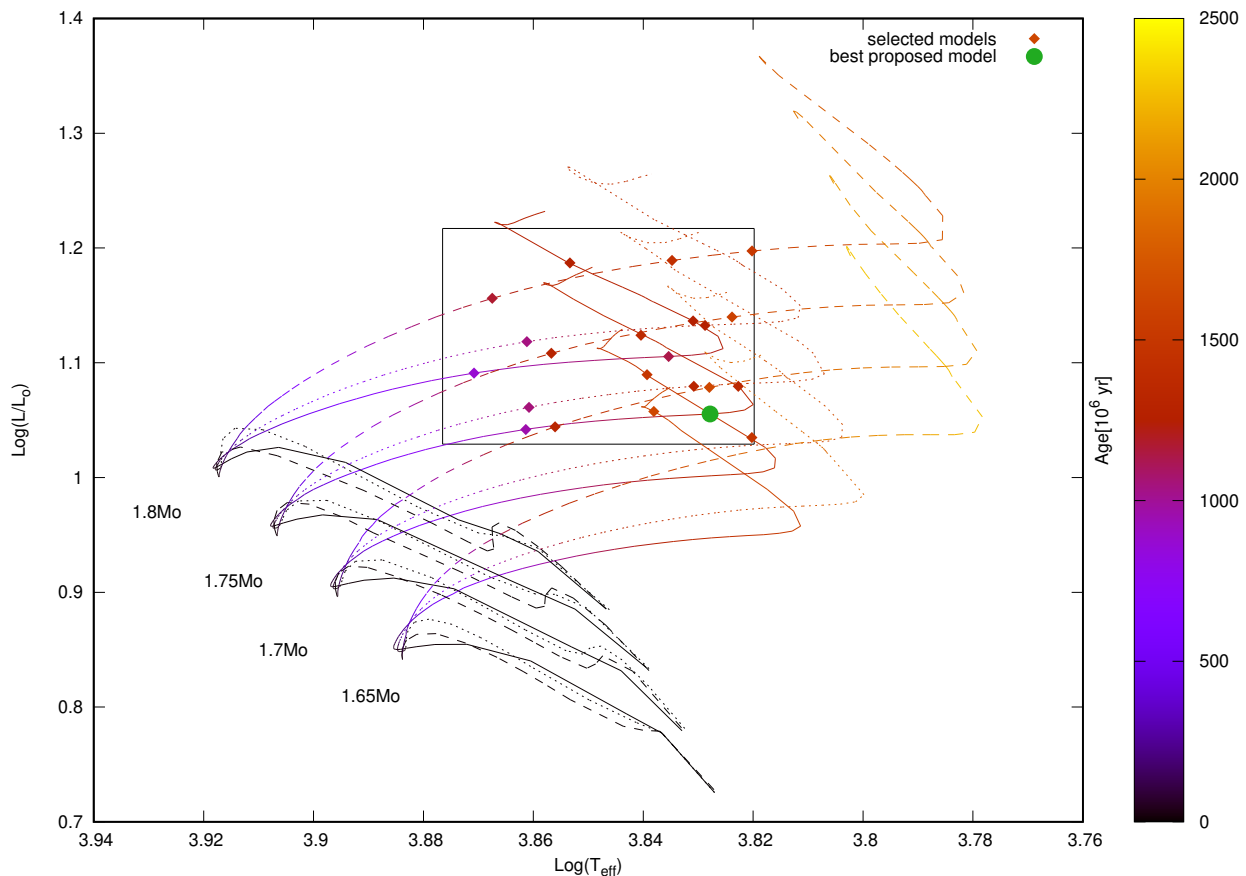


Fig. 11. HR diagram showing evolutionary sequences for different stellar masses. Sequences in solid lines correspond to cases without overshooting, those in short-dashed lines have $\alpha_{OV} = 0.1$ and long-dashed lines correspond to evolutionary sequences with $\alpha_{OV} = 0.3$. The box indicates the values of $\log(T_{\text{eff}})$ and $\log(L/L_{\odot})$ derived in Sect. 2. Colour coding shows the age of each evolutionary sequence. Selected models listed in Table 8 are shown by diamonds. The green circle shows the position of our best-fit model (see main text).

5.3. Asteroseismic analysis

The presence of a series of equidistant periods in CoRoT 102314644 (see Sect. 4.2) provides us with a useful tool for the search of a representative model: $\overline{\Delta\Pi}$, the mean period spacing of high order g -modes.

As stars evolve in the main sequence and consume H in the core, the Brunt-Väisälä (B-V) frequency, which governs the behaviour of g modes, is affected by the change of the convective core. For masses greater than $\sim 1.5M_{\odot}$, the core shrinks and its edge moves inward as the star evolves. The period can be expressed as:

$$\Pi_n \approx \frac{2\pi^2|n|}{\sqrt{l(l+1)}} \left[\int_a^b \frac{N}{r} dr \right]^{-1} \quad (5)$$

where N is the Brunt-Väisälä frequency, and a and b are the lower and upper boundary of the propagation zone of the g -mode. Thus, during the evolution, the integral increases since it expands toward inner regions resulting in a decreasing period and therefore a decreasing period spacing of g (see Miglio et al. 2008, for example).

We used this parameter as an indicator of the evolutionary status of stars at the main sequence (Saio et al. 2015; Kurtz et al. 2014; Sánchez Arias et al. 2017) which allowed

us to place constraints in the search for a representative model. For each model inside the box in Fig. 11, we calculate the mean period spacing of g -modes for $\ell = 1, 2$, as follows:

$$\overline{\Delta\Pi}_{\ell} = \frac{P_j - P_i}{n - 1} \quad (6)$$

where P_j and P_i are the closest periods to the extremes inside the observed interval [90878.5:98984.9] s where the asymptotic series lie; and n is the number of periods found in this range.

Table 8 summarizes the mass, the overshooting parameter, the age, $\overline{\Delta\Pi}_{\ell}$ and the difference between $\overline{\Delta\Pi}_{\ell}$ and the value found in Sect. 4.2 for modes with $\ell = 1$ and 2 for CoRoT 102314644.

Another parameter we employed to select our best model is the ratio between the period spacing for $\ell = 1$ and $\ell = 2$, which should be equal to $\sqrt{3}$ in the asymptotic regime. We also included this value in Table 8 for the selected models. We decided to use this criterion due to the possible deviation from the asymptotic regime with the adopted search. Our model was selected by the one with the lowest $D_{l=2}$ among those ones closest to $\frac{\overline{\Delta\Pi}_{l=1}}{\overline{\Delta\Pi}_{l=2}} = \sqrt{3}$. This model has $1.75M_{\odot}$, no core overshooting, 1241.24×10^6 yrs

and its luminosity and radius are $11.36L_{\odot}$ and $2.48R_{\odot}$. We notice that mode-trapping or other internal mode-selection mechanisms might prevent us from detecting more periods belonging to the observed asymptotic series resulting in a mean period spacing of g -modes apart from the asymptotic value.

Mass	Age	$\Delta\Pi_1$	D_1	$\Delta\Pi_2$	D_2	$\frac{\Delta\Pi_{\ell=1}}{\Delta\Pi_{\ell=2}}$
$[M_{\odot}]$	$[10^6 \text{ yr}]$	[s]	[s]	[s]	[s]	
1.65	1628.81	1662	41	1494	127	1.112
1.70	1480	3723	2102	1179	442	3.157
	1489.46	1334	287	792	829	1.684
1.70	1318.24	4062	2440	2085	464	1.948
$\alpha_{ov}=0.3$	1631.84	3858	2237	2333	712	1.653
1.75	955.35	2999	1378	2148	527	1.396
	1241.24	2313	692	1491	130	1.551
	1352.82	2425	804	1233	388	1.966
	1367.39	2040	419	1061	560	1.922
1.75	1052.77	3815	2194	1624	3	2.349
$\alpha_{ov}=0.1$	1315.38	2117	496	2161	540	0.979
1.75	1301.64	4177	2556	2428	807	1.720
$\alpha_{ov}=0.3$	1582.64	2799	1178	2086	465	1.341
1.80	869.37	2596	975	2201	580	1.179
	1134.88	4022	2401	1297	324	3.101
	1250.19	2330	709	1335	286	1.745
	1261.07	1595	26	1004	617	1.588
1.80	1041.9	3398	1777	1717	96	1.979
$\alpha_{ov}=0.1$	1266.84	2644	1023	2060	439	1.283
1.80	1175.14	2859	1238	2085	464	1.371
$\alpha_{ov}=0.3$	1429.6	3264	1643	2193	572	1.488
	1517.43	2814	1193	2562	941	1.098

Table 8. Mass, age, mean period spacing of g modes, the difference ($D_{\ell} = |\Delta\Pi - \Delta\Pi_{\ell}|$) with the observed one for $\ell = 1$ and 2 modes and the ratio $\frac{\Delta\Pi_{\ell=1}}{\Delta\Pi_{\ell=2}}$ for the selected models in our preliminary exploration indicated in Fig. 11. The uncertainty in $\Delta\Pi$ is on the order of 20s.

6. Summary and Conclusions

In this work, we have presented a detailed analysis of the light curve of CoRoT 102314644 and its frequencies. This star exhibits a rich frequency spectrum, with characteristics typical of hybrid δ Sct- γ Dor stars. Such objects offer a great opportunity to explore both the outer regions as well as their deep interior, due to the simultaneous presence of p and g modes. We performed an in-depth analysis of the frequency and variable content of the time series:

- We detected two separate frequency domains, corresponding to γ Dor domain and δ Sct type oscillations. We detected 26 pure frequencies in the γ -Dor range of $[0.32, 3.66]$ c/d, and 15 pure frequencies in the δ -Sct range $[9.38, 21.39]$ c/d (Fig. 3 and Tables A.1 and A.2).

- In the γ Dor domain, we found an asymptotic series of 6 equidistant periods with a mean separation of $1621\text{s} \pm 20\text{s}$ (Fig. 8 and Table 3) which most likely corresponds to $\ell = 2$.

- In the δ Sct domain, we found a quintuplet centred in the highest amplitude frequency of this domain, p_1 . The splitting in the frequencies of this quintuplet suggests that $f_{rot} = 0.32629$ c/d is a rotational frequency (Table 5).

- The phase diagram corresponding to f_{rot} (Fig 4) along with the moving bumps and the amplitude variation from one orbit to another in Fig. 5 suggest the presence of spots in this hybrid star, in the case of f_{rot} being a rotational frequency.

- Another remarkable characteristic of this hybrid star is the presence of coupling between p and g modes in the δ Sct domain (Table 7). This phenomenon, probably common among hybrid δ Sct- γ Dor stars, should provide information about their internal structure and the resonant cavities in these kinds of stars.

- We developed a preliminary modelling for CoRoT 102314644 by employing our frequency analysis along with the parameters derived in Sec. 2.2, corrected for extinction. We obtained a mass and age of $1.75M_{\odot}$ and 1241×10^6 yrs, without overshooting. The model parameters are $L = 11.36L_{\odot}$, $T_{\text{eff}} = 6726$ K, $R = 2.48R_{\odot}$ and mean period spacing $\Delta\Pi = 1624$ s, which of course reproduce the derived parameters in Sec. 2.2 within their uncertainties.

Finally, we highlight the need to follow up this star with spectroscopic measurements in order to detect orbital radial velocities deviations from a possible companion or width-line variations over a rotational period from a line corresponding to surface activity in the case of CoRoT 102314644 being a spotted star.

Acknowledgements. JPSA acknowledges the Henri Poincaré Junior Fellowship Program at the Observatoire de la Côte d’Azur. We thank the referee for their valuable time in reviewing the manuscript and providing suggestions for improvement. The Astronomical Institute Ondřejov is supported by the project RVO:67985815. This paper is dedicated to the memory of Eric Chapellier.

References

- Aerts, C., Christensen-Dalsgaard, J., & Kurtz, D. W. 2010, *Asteroseismology*
- Aerts, C., Mathis, S., & Rogers, T. M. 2019, *ARA&A*, 57, 35
- Alexander, D. R. & Ferguson, J. W. 1994, *ApJ*, 437, 879
- Angulo, C., Arnould, M., Rayet, M., et al. 1999, *Nuclear Physics A*, 656, 3
- Antoci, V., Cunha, M., Houdek, G., et al. 2014, *ApJ*, 796, 118
- Auvergne, M., Bodin, P., Boisnard, L., et al. 2009, *A&A*, 506, 411
- Baker, N. & Kippenhahn, R. 1962, *ZAp*, 54, 114
- Balona, L. A. 2014, *MNRAS*, 437, 1476
- Balona, L. A., Daszyńska-Daszkiewicz, J., & Pamyatnykh, A. A. 2015, *MNRAS*, 452, 3073
- Baran, A. S. & Koen, C. 2021, *Acta Astron.*, 71, 113
- Böhm-Vitense, E. 1958, *ZAp*, 46, 108
- Borucki, W. J. 2016, *Reports on Progress in Physics*, 79, 036901
- Bowman, D. M., Kurtz, D. W., Breger, M., Murphy, S. J., & Holdsworth, D. L. 2016, *MNRAS*, 460, 1970
- Bradley, P. A., Guzik, J. A., Miles, L. F., et al. 2015, *AJ*, 149, 68
- Casagrande, L., Lin, J., Rains, A. D., et al. 2020, *arXiv e-prints*, arXiv:2011.02517
- Catelan, M. & Smith, H. A. 2015, *Pulsating Stars*
- Chapellier, E. & Mathias, P. 2013, *A&A*, 556, A87
- Chapellier, E., Mathias, P., Weiss, W. W., Le Contel, D., & Debosscher, J. 2012, *A&A*, 540, A117
- Chowdhury, S., Joshi, S., Engelbrecht, C. A., et al. 2018, *Ap&SS*, 363, 260
- Claret, A. & Bloemen, S. 2011, *A&A*, 529, A75
- Danielski, C., Babusiax, C., Ruiz-Dern, L., Sartoretti, P., & Arenou, F. 2018, *A&A*, 614, A19
- Deleuil, M., Meunier, J. C., Moutou, C., et al. 2009, *AJ*, 138, 649
- Dupret, M.-A., Grigahcène, A., Garrido, R., Gabriel, M., & Scuflaire, R. 2004, *A&A*, 414, L17
- Fossat, E., Boumier, P., Corbard, T., et al. 2017, *A&A*, 604, A40
- Gaia Collaboration, Brown, A. G. A., Vallenari, A., et al. 2018, *A&A*, 616, A1

- Gaia Collaboration, Brown, A. G. A., Vallenari, A., et al. 2021, *A&A*, 649, A1
- Gaia Collaboration, Vallenari, A., Brown, A. G. A., et al. 2022, arXiv e-prints, arXiv:2208.00211
- Giles, H. A. C., Collier Cameron, A., & Haywood, R. D. 2017, *MNRAS*, 472, 1618
- Grevesse, N. & Sauval, A. J. 1998, *Space Sci. Rev.*, 85, 161
- Grigahcène, A., Antoci, V., Balona, L., et al. 2010, *ApJ*, 713, L192
- Grigahcène, A., Dupret, M.-A., Gabriel, M., Garrido, R., & Scuflaire, R. 2005, *A&A*, 434, 1055
- Gustafsson, B., Edvardsson, B., Eriksson, K., et al. 2008, *A&A*, 486, 951
- Guzik, J. A., Kaye, A. B., Bradley, P. A., Cox, A. N., & Neuforge, C. 2000, *ApJ*, 542, L57
- Handler, G., Balona, L. A., Shobbrook, R. R., et al. 2002, *MNRAS*, 333, 262
- Iglesias, C. A. & Rogers, F. J. 1996, *ApJ*, 464, 943
- Kaye, A. B., Handler, G., Krisciunas, K., Poretti, E., & Zerbi, F. M. 1999, *Publications of the Astronomical Society of the Pacific*, 111, 840
- Kennedy, J. R., Jefferies, S. M., & Hill, F. 1993, *Astronomical Society of the Pacific Conference Series*, Vol. 42, *Solar G-Mode Signatures in P-Mode Signals*, ed. T. M. Brown, 273
- Kurtz, D. W., Saio, H., Takata, M., et al. 2014, *MNRAS*, 444, 102
- Kurtz, D. W., Shibahashi, H., Murphy, S. J., Bedding, T. R., & Bowman, D. M. 2015, *MNRAS*, 450, 3015
- Lallement, R., Babusiaux, C., Vergely, J. L., et al. 2019, *A&A*, 625, A135
- Lenz, P. & Breger, M. 2005, *Communications in Asteroseismology*, 146, 53
- Li, G., Bedding, T. R., Murphy, S. J., et al. 2019, *MNRAS*, 482, 1757
- Lindegren, L., Bastian, U., Biermann, M., et al. 2021, *A&A*, 649, A4
- Miglio, A., Montalbán, J., Noels, A., & Eggenberger, P. 2008, *MNRAS*, 386, 1487
- Morel, P. & Lebreton, Y. 2008, *Ap&SS*, 316, 61
- Morris, S. L. 1985, *ApJ*, 295, 143
- Ouazzani, R.-M., Marques, J. P., Goupil, M.-J., et al. 2019, *A&A*, 626, A121
- Paunzen, E., Hümmerich, S., Bernhard, K., & Walczak, P. 2017, *MNRAS*, 468, 2017
- Reinhold, T., Reiners, A., & Basri, G. 2013, *A&A*, 560, A4
- Rogers, F. J., Swenson, F. J., & Iglesias, C. A. 1996, *ApJ*, 456, 902
- Saio, H., Kurtz, D. W., Murphy, S. J., Antoci, V. L., & Lee, U. 2018, *MNRAS*, 474, 2774
- Saio, H., Kurtz, D. W., Takata, M., et al. 2015, *MNRAS*, 447, 3264
- Sánchez Arias, J. P., Córscico, A. H., & Althaus, L. G. 2017, *A&A*, 597, A29
- Skarka, M., Žák, J., Fedurco, M., et al. 2022, *A&A*, 666, A142
- Solanki, S. K. 2003, *A&A Rev.*, 11, 153
- Tassoul, M. 1980, *ApJS*, 43, 469
- Townsend, R. H. D. & Teitler, S. A. 2013, *MNRAS*, 435, 3406
- Uytterhoeven, K., Moya, A., Grigahcène, A., et al. 2011, *A&A*, 534, A125
- Van Reeth, T., Tkachenko, A., & Aerts, C. 2016, *A&A*, 593, A120
- Xiong, D. R., Deng, L., Zhang, C., & Wang, K. 2016, *MNRAS*, 457, 3163

Appendix A: Tables

Table A.1. Complete list of stellar frequencies.

	Frequency [c/d]	$3\sigma_f$ [c/d]	A [mmag]	Φ	Ident
F_1	11.39107	0.00003	8.67	0.991	p_1
F_2	0.65259	0.00084	4.48	0.819	$2f_{rot}$
F_3	11.89972	0.00090	3.72	0.572	p_2
F_4	1.00595	0.00013	2.00	0.602	g_1
F_5	0.87286	0.00015	1.89	0.773	g_2
F_6	0.90251	0.00027	1.52	0.581	g_3
F_7	0.93445	0.00013	1.50	0.237	g_4
F_8	0.32629	0.00021	1.37	0.487	f_{rot}
F_9	0.88683	0.00905	1.22	0.686	g_5
F_{10}	11.25403	0.00020	1.16	0.117	p_3
F_{11}	11.41624	0.04119	1.10	0.280	p_4
F_{12}	1.15487	0.00024	0.992	0.872	g_6
F_{13}	2.76150	0.00034	0.864	0.769	g_7
F_{14}	0.95072	0.03840	0.843	0.852	g_8
F_{15}	0.36959	0.00035	0.822	0.450	g_9
F_{16}	1.57904	0.00032	0.767	0.31	g_{10}
F_{17}	3.5859	0.00033	0.746	0.5648	g_{11}
F_{18}	0.46385	0.00034	0.695	0.520	f_{spot}
F_{19}	10.73844	0.00037	0.667	0.150	$p_1 - 2f_{rot}$
F_{20}	1.36005	0.00040	0.584	0.943	g_{12}
F_{21}	2.86648	0.00151	0.572	0.075	g_{13}
F_{22}	3.66310	0.00047	0.557	0.915	g_{14}
F_{23}	22.78214	0.00043	0.539	0.407	$2p_1$
F_{24}	13.34339	0.00046	0.519	0.995	p_5
F_{25}	0.66913	0.00020	0.493	0.900	g_{15}
F_{26}	0.61232	0.00030	0.483	0.822	g_{16}
F_{27}	0.39653	0.00054	0.480	0.011	g_{17}
F_{28}	2.88476	0.00134	0.464	0.306	g_{18}
F_{29}	9.38571	0.00077	0.444	0.861	p_6
F_{30}	0.57377	0.00046	0.443	0.997	g_{19}
F_{31}	1.04855	0.00053	0.422	0.368	g_{20}
F_{32}	0.91855	0.00582	0.388	0.207	g_{21}
F_{33}	0.50955	0.01043	0.356	0.974	g_{22}
F_{34}	2.65892	0.00203	0.351	0.711	g_{23}
F_{35}	0.42446	0.00116	0.348	0.103	g_{24}
F_{36}	0.52895	0.00119	0.345	0.805	g_{25}
F_{37}	12.63590	0.00087	0.310	0.480	p_7
F_{38}	23.29078	0.000832	0.306	0.938	$p_1 + p_2$
F_{39}	0.98517	0.00012	0.2952	0.979	g_{26}
F_{40}	10.89784	0.00110	0.288	0.506	$p_2 - g_1$
F_{41}	11.67328	0.00117	0.228	0.292	p_8
F_{42}	12.41205	0.00128	0.180	0.946	p_9
F_{43}	5.03888	0.00141	0.173	0.259	i_1
F_{44}	10.93192	0.00338	0.167	0.019	p_{10}
F_{45}	11.24675	0.00020	0.145	0.401	$p_2 - 2f_{rot}$
F_{46}	22.64486	0.00172	0.143	0.363	$p_1 + p_3$
F_{47}	12.04353	0.02686	0.132	0.209	$p_1 + 2f_{rot}$
F_{48}	22.80735	0.00998	0.124	0.498	$p_1 + p_4$
F_{49}	10.51816	0.00280	0.115	0.095	$p_1 - g_2$
F_{50}	10.38536	0.00418	0.113	0.166	$p_1 - g_1$
F_{51}	10.76353	0.13835	0.105	0.134	$p_4 - 2f_{rot}$
F_{52}	23.79931	0.0020	0.102	0.866	$2p_2$
F_{53}	14.92732	0.01083	0.0963	0.018	p_{11}
F_{54}	12.26440	0.00355	0.096	0.298	$p_1 + g_2$
F_{55}	12.39788	0.03299	0.092	0.707	$p_1 + g_1$
F_{56}	13.79589	0.00674	0.0906	0.073	p_{12}
F_{57}	10.45718	0.00412	0.0881	0.439	$p_1 - g_4$
F_{58}	11.71775	0.01550	0.0867	0.297	$p_1 + f_{rot}$
F_{59}	8.62954	0.00577	0.0848	0.996	$p_1 - g_7$

Table A.2. Complete list of stellar frequencies. Continuation.

	Frequency [c/d]	$3\sigma_f$ [c/d]	A [mmag]	Φ [rad]	Ident
F_{60}	12.29424	0.02011	0.0836	0.419	$p_1 + g_3$
F_{61}	14.45601	0.01786	0.0832	0.897	p_{13}
F_{62}	10.48902	0.03187	0.0808	0.448	$p_1 - g_3$
F_{63}	11.06506	0.00386	0.0785	0.036	$p_1 - f_{rot}$
F_{64}	23.15392	0.00982	0.0692	0.378	$p_2 + p_3$
F_{65}	14.89416	0.03191	0.0656	0.415	p_{14}
F_{66}	24.73414	0.02992	0.0540	0.560	$p_1 + p_5$
F_{67}	22.12889	0.06772	0.0423	0.745	$2p_1 - 2f_{rot}$
F_{68}	21.39415	0.05756	0.040	0.071	p_{15}